

PAPER • OPEN ACCESS

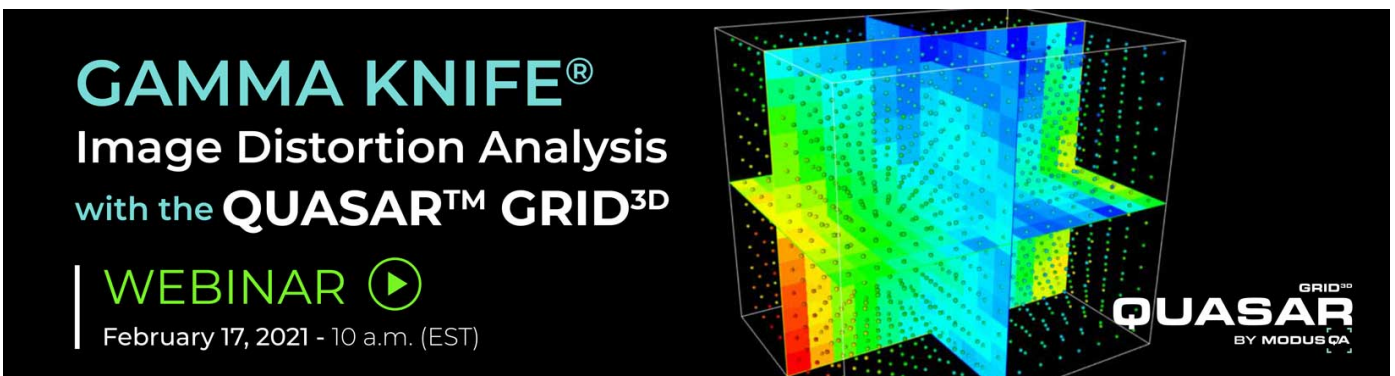
# Super-resolution x-ray phase-contrast and dark-field imaging with a single 2D grating and electromagnetic source stepping

To cite this article: Kristian R Rix *et al* 2019 *Phys. Med. Biol.* **64** 165009

View the [article online](#) for updates and enhancements.

## Recent citations

- [High sensitivity X-ray phase contrast imaging by laboratory grating-based interferometry at high Talbot order geometry](#)  
Joan Vila-Comamala *et al*
- [Tracking based, high-resolution single-shot multimodal x-ray imaging in the laboratory enabled by the sub-pixel resolution capabilities of the MÖNCH detector](#)  
E. S. Dreier *et al*
- [Super-resolution X-ray imaging with hybrid pixel detectors using electromagnetic source stepping](#)  
T. Dreier *et al*



**GAMMA KNIFE®**  
Image Distortion Analysis  
with the **QUASAR™ GRID<sup>3D</sup>**

**WEBINAR** 

February 17, 2021 - 10 a.m. (EST)

**QUASAR**  
BY MODUSCA  
GRID<sup>3D</sup>

## OPEN ACCESS



## PAPER

## Super-resolution x-ray phase-contrast and dark-field imaging with a single 2D grating and electromagnetic source stepping

RECEIVED  
5 November 2018REVISED  
20 June 2019ACCEPTED FOR PUBLICATION  
8 July 2019PUBLISHED  
14 August 2019

Original content from this work may be used under the terms of the [Creative Commons Attribution 3.0 licence](https://creativecommons.org/licenses/by/3.0/).

Any further distribution of this work must maintain attribution to the author(s) and the title of the work, journal citation and DOI.

Kristian R Rix<sup>1,4</sup>, Till Dreier<sup>2,3,4</sup> , Tao Shen<sup>2,6</sup> and Martin Bech<sup>2,5</sup><sup>1</sup> University of Copenhagen, Niels Bohr Institute, x-ray and Neutron Science, 2100 Copenhagen, Denmark<sup>2</sup> Department of Medical Radiation Physics, Clinical Sciences Lund, Lund University, 221 85 Lund, Sweden<sup>3</sup> Excillum AB, Jan Stenbecks Torg 17, 164 40 Kista, Sweden<sup>4</sup> These authors contributed equally.<sup>5</sup> Author to whom any correspondence should be addressed.<sup>6</sup> Current address: Karlsruher Institut für Technologie (KIT), 76131 Karlsruhe, GermanyE-mail: [martin.bech@med.lu.se](mailto:martin.bech@med.lu.se)**Keywords:** x-ray imaging, dark field, differential phase contrast, movable micro focus x-ray source, single exposure imaging, super resolutionSupplementary material for this article is available [online](#)**Abstract**

Here we report a method for increased resolution of single exposure three modality x-ray images using super-resolution. The three x-ray image modalities are absorption-, differential phase-contrast-, and dark-field-images. To create super-resolution, a non-mechanically movable micro-focus x-ray source is used. A series of almost identical x-ray projection images is obtained while the point source is translated in a two-dimensional grid pattern. The three image modalities are extracted from fourier space using spatial harmonic analysis, also known as the single-shot method. Using super-resolution on the low-resolution series of the three modalities separately results in high-resolution images for the modalities. This approach allows to compensate for the inherent loss in resolution caused by the single-shot method without increasing the need for stability or algorithms accounting for possible motion.

**1. Introduction**

The development of x-ray imaging setups has accelerated over the last decade. Improvements in x-ray microscopy and Talbot–Lau grating interferometers (Momose *et al* 2003, David *et al* 2002)—with hardware such as micro- and nano-focus x-ray tubes have been a catalyst for this. Also, different imaging modalities like differential phase-contrast (DPC) achieved with the coded-aperture technique by Olivo and Speller (2007) and dark-field (DF) imaging achieved using synchrotron radiation and a misaligned analyzer crystal by Chapman *et al* (1997) and Arfelli *et al* (2000), which was later realized using a Talbot–Lau interferometer by Pfeiffer *et al* (2008) have become available in the laboratory.

In most imaging applications, the image quality is evaluated by resolution and contrast as the most important factors. Thus, enhancement of image resolution and contrast is an ongoing process by optimizing and developing appropriate hardware and software. Using the Talbot interferometer as a base, new enhancements have recently been developed, e.g. a motionless electromagnetic phase stepping approach was demonstrated by Harmon *et al* (2015). Other closely related methods such as Speckle-based imaging described by Bérújon *et al* (2012), the single-shot method developed by Wen *et al* (2010), and the method described by Diemoz *et al* (2011) utilizing two line gratings can be categorized as non-scanning techniques. Here we present a method to enhance the resolution using the single-shot method combined with electromagnetic source stepping to create super-resolution.

**2. Methods and setup**

Our method is a combination of three well documented procedures: *spatial harmonic analysis* (SHA) or single-shot imaging (Wen *et al* 2010), 2D electromagnetic source stepping similar to the approach of Harmon *et al*

(2015), and image enhancement using super-resolution. However, there are several similarities to the coded aperture method described by Olivo and Speller (2007).

The SHA method achieves DPC and DF imaging via a 2D absorption grating and a micro-focus source, eliminating the need for a source grating. x-ray refraction and diffraction in a sample are measured as variations in the 2D intensity pattern created by the grating. This is accomplished in Fourier space, where the information of the refraction and diffraction is represented in the 1st-order harmonics from which phase-contrast and dark-field, i.e. diffraction, information are extracted. Absorption contrast can be extracted from the 0th-order harmonic.

Motionless electromagnetic phase stepping described by Harmon *et al* (2015) is a variation of the Talbot–Lau interferometer. In Talbot–Lau interferometry, a combination of three gratings create a fringe pattern on the detector. By stepping one of the gratings and acquiring three or more images, the DPC and DF images can be reconstructed. In the motionless electromagnetic phase stepping approach, mechanical stepping of the grating is replaced by electromagnetic source point stepping in 1D, effectively creating the same image modalities as mechanical stepping. Here we utilize an Excillum micro-focus source with 2D stepping capabilities.

The approach presented by Olivo and Speller (2007) utilizes a line grating and a detector mask added directly onto the detector assuring the individual beams do not overlap on the detector. To overcome the loss in resolution, the authors move the sample and combine the images. Contrary to the method described by Chapman *et al* (1997), neither a perfect crystal nor monochromatic x-rays are required. Moreover, the authors propose an aperture to achieve the same results in 2D as well. Our method relies on a single 2D structure and does not require to add a structure directly onto the detector.

Super-resolution is a mathematical method using a series of slightly shifted low-resolution images to estimate one high-resolution image. Each individual image is interpolated on a finer high-resolution grid (Gilman *et al* 2008) and registered with sub-pixel precision (Guizar-Sicairos *et al* 2008). The resulting images are then combined into a single high-resolution image. Finally, the estimated high-resolution image is deblurred. Commonly, deconvolution is used such as a Wiener filter, Richardson–Lucy filter, image regularization, or blind deconvolution (Milanfar 2010, Yadav *et al* 2016). Alternatively, more complex algorithms such as iterative back-projection as proposed by Irani and Peleg (1991) or *projection onto convex sets* (POCS) as proposed by Greenspan (2008) can be implemented. However, though all algorithms perform well in their specific scenario, not every algorithm is suited for every imaging setup and sample. Therefore, we decided to employ a simple more generalized approach to super-resolution as described by Gilman *et al* (2008) and Milanfar (2010).

The x-ray spot is calibrated to 10  $\mu\text{m}$  *full width at half maximum* (FWHM) at an acceleration voltage of 70 kV. Furthermore, two additional components are used in this setup, illustrated in figure 1(a). A 2D gold grating with checker-board pattern of 36  $\mu\text{m}$  pitch and 160  $\mu\text{m}$  thickness (Microworks GmbH) is used as a coded aperture. As detector, a Pilatus 100K hybrid pixel detector from Dectris Ltd. with a pixel size of 172  $\mu\text{m}$  is used. These components define the used geometry: the grating is placed 8 cm from the source and the detector is placed 1.45 m away from the grating so the grating period corresponds to an area of  $4 \times 4$  pixels on the detector. The sample position depends on the desired magnification. Highest angular sensitivity is achieved when placing the sample as close to the grating as possible (Donath *et al* 2009).

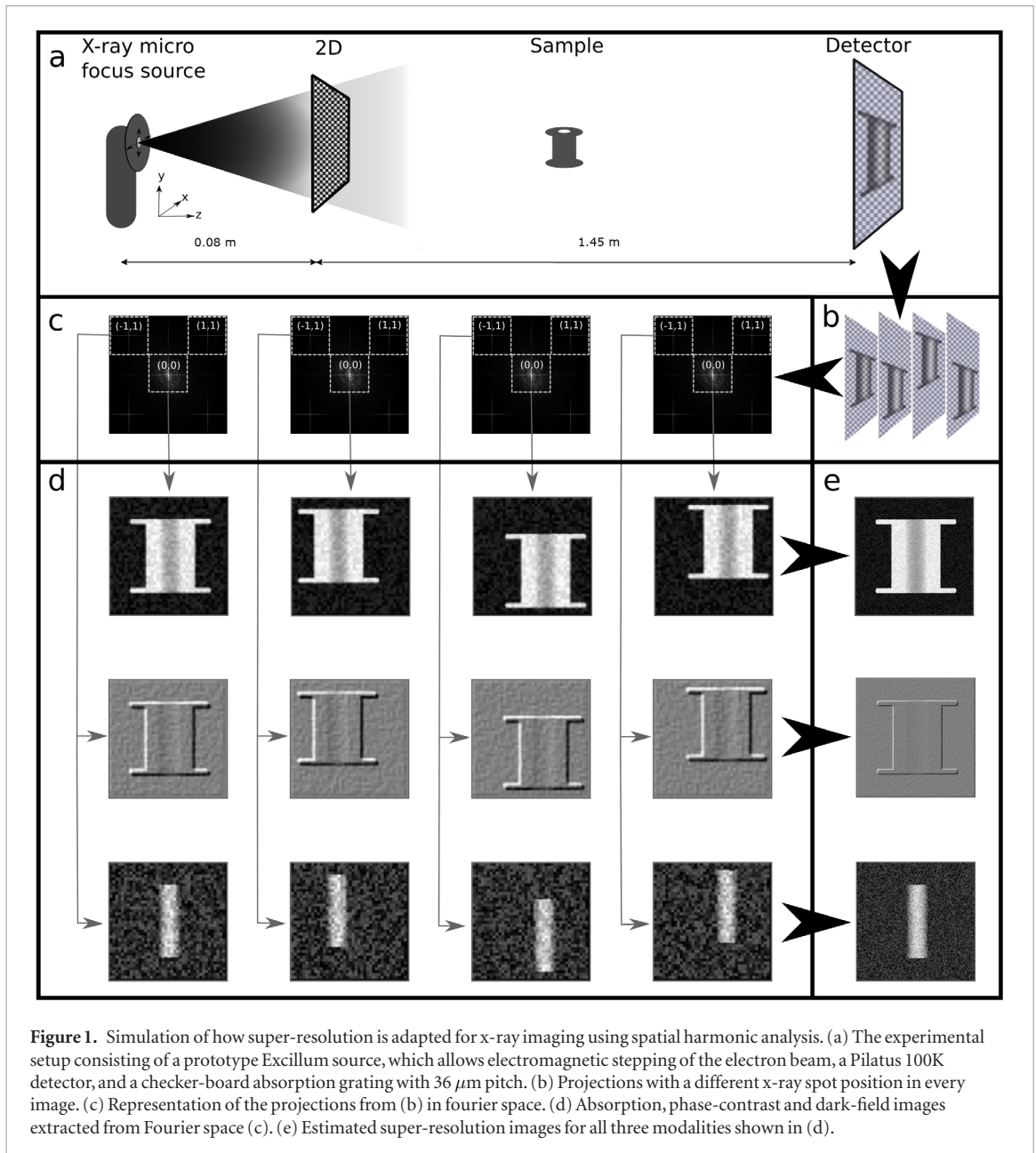
## 2.1. Single-shot x-ray phase-contrast imaging

Single-shot imaging allows to extract all three image modalities from a single exposure. However, this comes at the expense of resolution compared to multi-exposure scanning methods such as interferometry (Pfeiffer *et al* 2008) or Speckle-based imaging (Zanette *et al* 2014). The single-shot method utilises numerical fourier transforms on the recorded projections. Illustrations of such a transformation is shown in figure 1(c). The 0th-order harmonic contains the absorption information, which is retrieved by extracting the area with the harmonic in its center. The area size is defined by the number of pixels the grating period extends over. In our setup the full grating period spans  $4 \times 4$  pixels. The projection image is  $195 \times 487$  pixels, thus the Fourier transform of the image has to be split into  $4 \times 4$  equally sized regions resulting in  $48.75 \times 121.75$  pixels per area. This is the maximum size considered to be the limit where there is no overlap between 0th- and 1st-order harmonic information as illustrated in figure 1(c). Moreover, the area size has to be reduced further assuring the maximum to be the area's center pixel (Wen *et al* 2010).

The absorption image  $I_{abs}$  is created from the absolute value of the inverse fourier transform of the 0th-order harmonic. Further, the image is normalized with a reference image, containing only the grating, calculated in the same manner to retrieve the absorption image:

$$I_{abs} = -\ln \left( \frac{\mathcal{F}^{-1}[S_{(0,0),s}]}{\mathcal{F}^{-1}[S_{(0,0),r}]} \right). \quad (1)$$

Here  $[S_{(0,0),s}]$  and  $[S_{(0,0),r}]$  are the extracted 0th-order harmonics of the measurements with sample (s) and reference (r) respectively. Correction with a reference image is the same approach employed in Talbot



interferometer setups (Pfeiffer *et al* 2007). Further, the result is linearized to the sample thickness by applying the natural logarithm (Wen *et al* 2010). Evidently, the resolution of the absorption image is reduced by a factor determined by the grating period projected on the detector. Considering the *point spread function* (PSF) of the detector, a sufficient amount of pixels has to be selected to be able to resolve the interference pattern during data analysis. Moreover, it has to be noted that a reference image is required for every position of the x-ray spot, since the grating will be translated as well when moving the x-ray spot.

The 1st-order harmonics contain phase-information in perpendicular directions. Due to the characteristics of the grating (checker-board pattern), the discrete peaks in the 1st-order spatial frequency domain are at positions  $(-1, 1)$  and  $(1, 1)$  as illustrated in figure 1(c). Subsequently, the phase-contrast is sensitive in one of the two diagonals depending on the selected 1st-order harmonics. Due to the symmetry of the Fourier transformation, the information in  $(-1, 1)$  is identical to  $(1, -1)$  and  $(1, 1)$  is equivalent to  $(-1, -1)$ . By defining an area with the 1st-order harmonics in the centre, maximum non-overlapping information are extracted as illustrated in figure 1(c). The DPC-image  $I_{DPC}$  is then retrieved by applying the inverse Fourier transformation on the selected area with and without sample, subtracting the angle information in both images, and wrapping the result to  $\pi$ :

$$I_{DPC} = \angle(\mathcal{F}^{-1}[S_{(-1,1),s}] - \mathcal{F}^{-1}[S_{(-1,1),r}]). \quad (2)$$

Where  $[S_{(-1,1),s}]$  and  $[S_{(-1,1),r}]$  are the 1st-order harmonic peaks with sample and reference measurement respectively and  $\angle$  is the angle of the complex number.

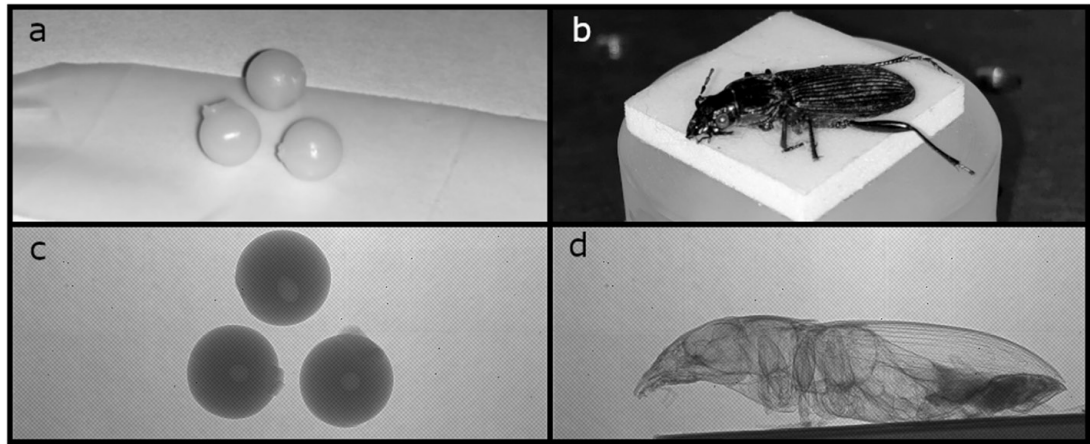


**Figure 2.** The used samples and their corresponding raw data. (a) Polymer spheres with a diameter of 6 mm. (b) A beetle fixated on tape. (c) Image obtained with the Pilatus detector of sample (a). (d) Image obtained with the Pilatus detector of sample (b).

The DF-image is calculated from the ratio between the 1st-order and 0th-order harmonics corrected with their corresponding reference image and linearized to the sample thickness. Since the 0th-order harmonic peak is assumed to not contain grating modulation, i.e. it is unaffected by refraction and diffraction, but affected by absorption and scattering (Wen *et al* 2010, Pfeiffer *et al* 2008), the dark-field-image  $I_{DF}$  can be calculated:

$$I_{DF} = -\ln \left( \frac{\mathcal{F}^{-1}[S_{(-1,1),s}] \cdot \mathcal{F}^{-1}[S_{(0,0),r}]}{\mathcal{F}^{-1}[S_{(-1,1),r}] \cdot \mathcal{F}^{-1}[S_{(0,0),s}]} \right). \quad (3)$$

Where  $[S_{(-1,1),s/r}]$  represents 1st-order harmonic peaks and  $[S_{(0,0),s/r}]$  represents 0th-order harmonic peaks with sample (s) or without sample (r). Illustrations of absorption, phase-contrast and dark-field images are provided in figure 1(d).

## 2.2. Super-resolution

Using a hybrid pixel detector as opposed to a CMOS or CCD camera has a fundamental advantage—no interactions between individual pixels, i.e. the detector's PSF is a single pixel and can therefore be neglected. This allows to choose a geometry projecting the grating period on an area of  $4 \times 4$  pixels reducing the resolution only by a factor of 4. Typically, images are deblurred using the PSF, which is unnecessary when using hybrid pixel detectors. Moreover, the magnified size of the x-ray spot on the detector is smaller than 1 pixel and, therefore, can be neglected as well. Thus, the resulting image quality depends essentially on the quality of the interpolated low-resolution images (Gilman *et al* 2008) and the precision of the registered shifts between images (Guizar-Sicairos *et al* 2008).

The *signal-to-noise ratio* (SNR) for absorption images is obtained by comparing a region without sample of the image with a reference image and multiplying by ten times the logarithm to base ten to obtain a result in dB. For dark-field images, the *contrast-to-noise ratio* (CNR) is used, which is defined as:

$$CNR = \frac{|M_s - M_{ref}|}{\sigma_{ref}}. \quad (4)$$

Where  $M_s$  and  $M_{ref}$  represent the mean value of a certain region with and without sample respectively and  $\sigma_{ref}$  is the standard deviation of the latter region. The regions are  $32 \times 32$  pixels in size and were manually chosen. The setup used is illustrated in figure 1(a). The arrows on the source indicates that the point source is movable. With the used Excillum source, it is possible to precisely move the electron beam, hence shifting the grid pattern of x-ray spots. Spacing of the x-ray spot stepping is calculated to assure a fixed translation of the sample on the detector. This guarantees sufficient additional information in the individual low-resolution images. For the described experiments, 16 images with a total shift of three pixels in  $x$  and  $y$  direction are used, the exposure time is 60 s, and the resolution is increased by a factor of 4. As samples (figure 2), we use polymer spheres with a diameter of 6 mm placed 0.6 m away from the source and a beetle placed 0.4 m away from the source.

## 3. Results

Here two different samples and the corresponding raw data are illustrated. Three polymer spheres are shown in figure 2(a) with their corresponding raw data obtained with a Pilatus detector in figure 2(c) and a beetle shown

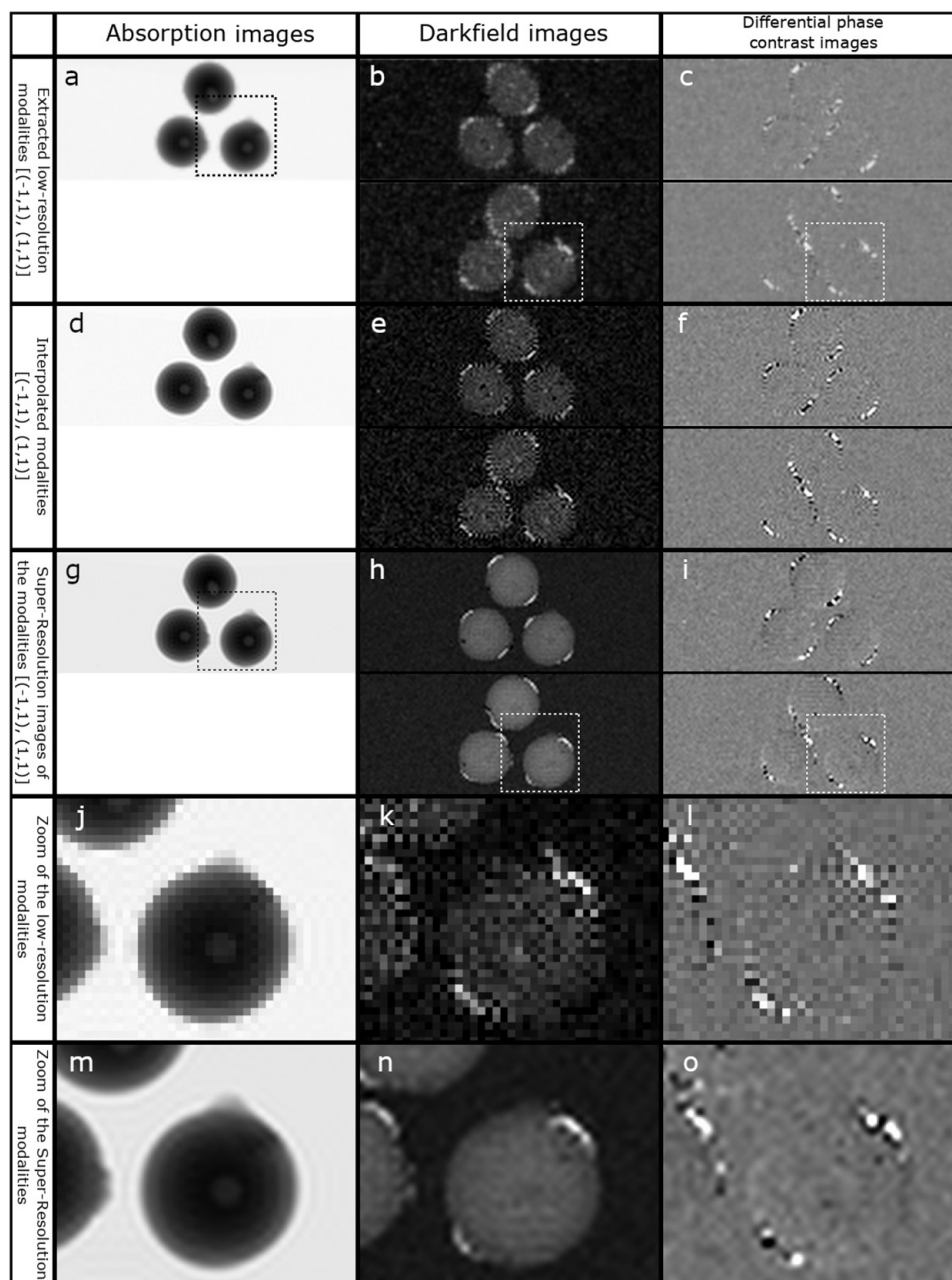


**Figure 3.** Extracted modalities and estimated super-resolution images of plastic spheres showing that the concept works as expected. The contrast has been adjusted for better comparability. (a) One extracted absorption image. (b)–(c) One extracted dark-field and phase-contrast image for region (-1,1) and (1,1) respectively. (d)–(f) Interpolated images corresponding to (a)–(c) using 4 times interpolation using a spline. (g)–(i) Estimated super-resolution images corresponding to the interpolated images in (d)–(f). (j)–(l) Zoom of the extracted images in (a)–(c). (m)–(o) Zoom of the estimated super-resolution images in (g)–(i).

in figure 2(b) with its corresponding raw data in figure 2(d). The polymer spheres are used to show that the principle works and the beetle is used to show that the method also works on more complex samples. Results from the polymer spheres and the beetle are shown in figures 3 and 4 respectively.

For the dark-field and phase-contrast modalities, two images can be extracted from regions  $(-1, 1)$  and  $(1, 1)$  on top and bottom respectively. Evidently, the resolution of the extracted modalities (figures 3(a)–(c)) is low, due to the single-shot method. However, interpolating (figures 3(d)–(f)) the images and combining them using super-resolution (figures 3(g)–(i)) improves the images notably. Comparing the low-resolution images to the super-resolution enhanced images shows an improved contrast and more details (figures 3(j)–(o)). It can be observed that the outline of the spheres is improved in enhanced images and an air bubble enclosed in the center of the spheres is visible in all modalities.

Similar to the DF-images, the DPC-images show a distinctive signal in the direction corresponding to the fourier direction. Both modalities show diagonal features in both directions perpendicular to each other. Region  $(-1, 1)$  shows features oriented at  $-45^\circ$ , while features in region  $(1, 1)$  are oriented at  $45^\circ$ .

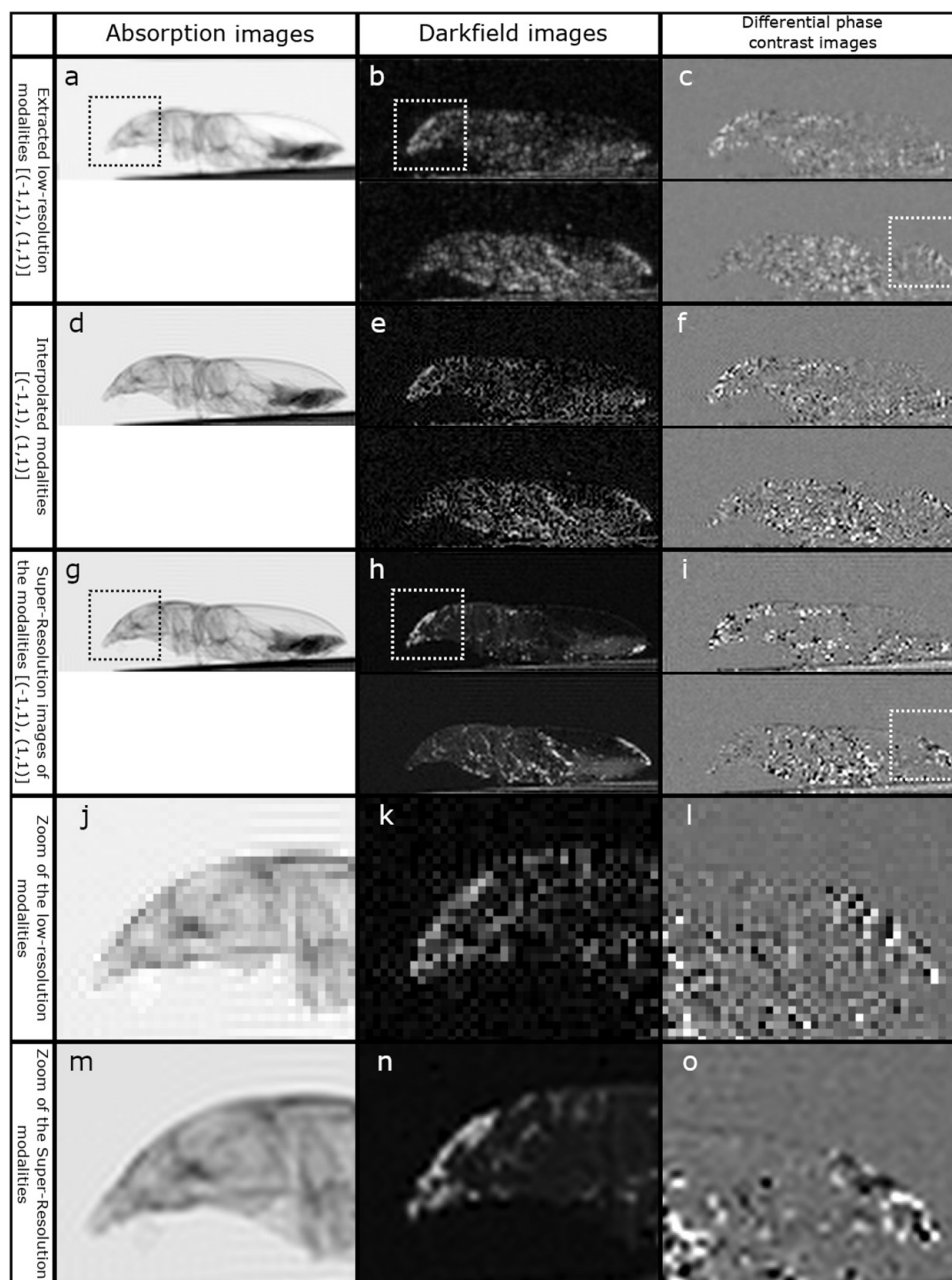


**Figure 4.** Extracted modalities and estimated super-resolution images of a beetle. The contrast has been adjusted for better comparability. (a) One extracted absorption image. (b)–(c) One extracted dark-field and phase-contrast image for region  $(-1,1)$  and  $(1,1)$  respectively. (d)–(f) Interpolated images corresponding to (a)–(c) using four times interpolation using a spline. (g)–(i) Estimated super-resolution images corresponding to the interpolated images in (d)–(f). (j)–(l) Zoom of the extracted images in (a)–(c). (m)–(o) Zoom of the estimated super-resolution images in (g)–(i).

The beetle sample shown in figure 4 is treated in the same way as the polymer spheres. Comparing the obtained absorption modality (figures 4(j) and (m)) shows a significant improvement of the insect's head. Both, outline and structure, are significantly improved and artefacts around the head, which are caused by the grating, are reduced. The enhanced dark-field images show the most significant improvements (figure 4(h)) as they allow to clearly observe the directional information in this modality. In the upper image (region  $(-1, 1)$ ), details in the head can be observed (zoom in figure 4(n)), while the lower image (region  $(1, 1)$ ) shows additional information in the middle section of the insect. This shows that, using the super-resolution approach, the amount of observable details in a sample can be increased.

Similar to the enhanced DF-images, the enhanced DPC-images also show clearer features inside the beetle and a clearer outline. However, the improvement is not as dramatic as observed for the DF-images.

Comparing the super-resolution enhanced images with the same amount of images without movements of the x-ray spot treated in the same way shows that the improvement of the absorption modality is largely due to interpolation. However, features in the super-resolution image (figure 5(a)) are clearer, the contrast is better,

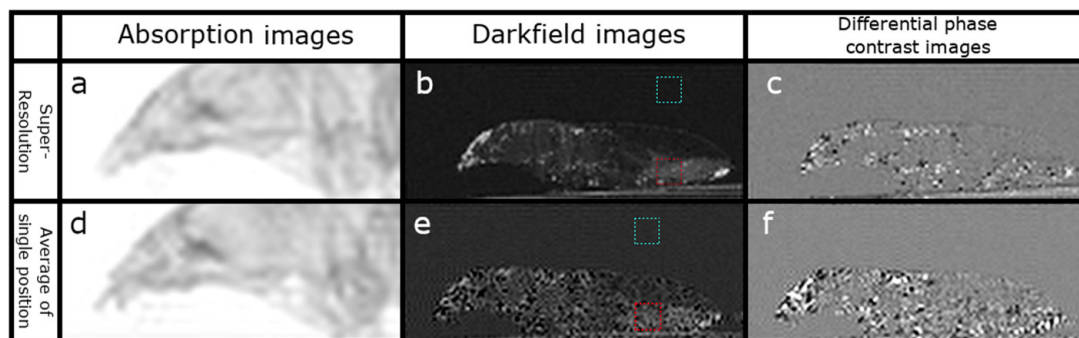


**Figure 5.** Comparison of super-resolution images and the same amount of interpolated images with 60s exposure time without x-ray spot movements. The contrast has been adjusted for better comparability. (a) Super-resolution absorption image of a beetle zoomed in on the head. (b) Super-resolution dark-field image of the beetle, where the regions used for CNR calculations are highlighted. (c) Super-resolution phase-contrast image of the beetle. (d) Averaged absorption image using a single x-ray spot position corresponding to (a). (e) Averaged dark-field image using a single x-ray spot position corresponding to (b), where the regions used for CNR calculations are highlighted. (f) Averaged phase-contrast image using a single x-ray spot position corresponding to (c).

and artefacts in the image are reduced compared to averaging non-translated images (figure 5(d)). For this comparison, the same exposure time (60 s) is used, i.e. the only difference is that the x-ray spot is not moved. In both cases, the number of detected photons reaching the detector is almost equal at  $5.29 \cdot 10^{10}$  and  $5.47 \cdot 10^{10}$  for super-resolution and a single position respectively. The super-resolution method requires one reference image (flat-field) per position (adding another  $6.13 \cdot 10^{10}$  photons), however, averaging images from the same position can be done with a few or even a single flat-field image. The presented case uses four flat-field images (adding another  $9.98 \cdot 10^9$  photons).

Moreover, a significant increase in details and sharpness can be observed for the DF-image shown in figure 5(b) compared to averaging images (figure 5(e)). The same effect can be observed for the DPC-images (figures 5(c) and (f)), but to a lesser degree. For this comparison the images without translation of the x-ray spot have been treated in exactly the same way as the super-resolution enhanced images.

The SNR of the super-resolution enhanced image (figure 5(a)) was measured to be 15.9 dB, while the SNR of the averaged images (figure 5(d)) was measured to be slightly lower at 15.16 dB. For the DF images (figures 5(b) and (e)), the CNR is used yielding 21.14 and 13.47 for the super-resolution enhanced image and the averaged images respectively. Considering the DPC images (figures 5(c) and (f)), SNR and CNR are not calculated since these methods are not well defined in this case. Intensity profiles of images displayed in figure 5 can be found in the supplementary online figure ([stacks.iop.org/PMB/64/165009/mmedia](https://stacks.iop.org/PMB/64/165009/mmedia)). In this case, the exposure time was long (60 s), i.e. sufficient photon statistics could be obtained and the SNR did not get worse compared to averaging non-shifted images with approximately an equivalent amount of photons per image.

#### 4. Discussion and conclusion

It is possible to generate high resolution DPC and DF images with very precise stepping setups, such as the Talbot–Lau interferometer. However due to the relative alignment between the gratings in these systems, the sensitivity from vibrations and different kinds of drift is substantial. The single-shot method is a simplified approach neglecting this issue, since no mechanical movements and only a single grating are required. Moreover, it takes inspiration from the coded-aperture method, but does not require to add a mask onto the detector. The main drawback of this method is a drastic reduction of resolution compared to the stepping setups.

In this paper, we demonstrated that loss in resolution can be overcome to a certain degree via super-resolution without increasing the demand for stability. Further, there is no need to account for grating instabilities via algorithms. Considering the coded-aperture approach, our approach is even simpler as it utilizes a single grating, thus relative movements between mask and grating do not have to be considered. Furthermore, both methods apply the idea of super-resolution to overcome a loss in resolution by the respective method. We expect that it is possible to further improve the images adapting a more advanced super-resolution method specifically adjusted for a concrete type of sample.

Recovering the modalities from images with a limited amount of photons will negatively affect the SNR of these images. This limitation is exacerbated by combining several SNR-limited images, thus reducing the SNR or limiting the SNR increase compared to scanning methods. However, the presented case has shown an improved SNR compared to averaging the same amount of non-shifted images using the same exposure time at the same

distance resulting in approximately the same number of photons for both cases. It has to be kept in mind that the used exposure time was relatively long providing sufficient photon statistics.

The presented method is very reliable as it is unaffected by short and long term instabilities and thermal drifts. This approach is based on geometric changes between images, which are processed individually. The sample translation can be adjusted by increasing or decreasing the deflection of the electron beam and it also depends on the sample position. However, very high deflection yields the risk of the x-ray spot shape changing, which can cause blurring and artefacts in the images. Thus, placing the samples even closer to the grating will reduce the deflection need to translate the sample for a specific amount of pixels and thereby also guarantee that the x-ray spot shape does not change.

## Acknowledgments

This project is financially supported by the Swedish Foundation for Strategic Research (SSF) Grant No. ID17-0097 and by the Swedish Research Council Grant No. E0605401 and E0605402.

## ORCID iDs

Till Dreier  <https://orcid.org/0000-0002-6632-402X>

## References

- Arfelli F *et al* 2000 Mammography with synchrotron radiation: phase-detection techniques *Radiology* **215** 286–93
- Bérubon S *et al* 2012 Two-dimensional x-ray beam phase sensing *Phys. Rev. Lett.* **108** 158102
- Chapman D *et al* 1997 Diffraction enhanced x-ray imaging *Phys. Med. Biol.* **42** 2015–25
- David C *et al* 2002 Differential x-ray phase contrast imaging using a shearing interferometer *Appl. Phys. Lett.* **81** 3287–9
- Diemoz P C *et al* 2011 A simplified approach for computed tomography with an x-ray grating interferometer *Opt. Express* **19** 1691
- Donath T *et al* 2009 Inverse geometry for grating-based x-ray phase-contrast imaging *J. Appl. Phys.* **106** 054703
- Gilman A, Bailey D G and Marsland S R 2008 Interpolation models for image super-resolution *4th IEEE Int. Symp. on Electronic Design, Test and Applications (delta 2008)* (Hong Kong: IEEE) pp 55–60
- Greenspan H 2008 Super-resolution in medical imaging *Comput. J.* **52** 43–63
- Guizar-Sicairos M, Thurman S T and Fienup J R 2008 Efficient subpixel image registration algorithms *Opt. Lett.* **33** 2 156
- Harmon K J *et al* 2015 Motionless electromagnetic phase stepping versus mechanical phase stepping in x-ray phase-contrast imaging with a compact source *Phys. Med. Biol.* **60** 3031–43
- Irani M and Peleg S 1991 Improving resolution by image registration *CVGIP, Graph. Models Image Process.* **53** 231–9
- Milanfar P 2010 *Super-Resolution Imaging* 1st edn (Boca Raton, FL: CRC Press) (<https://doi.org/10.1201/9781439819319>)
- Momose A *et al* 2003 Demonstration of x-ray talbot interferometry *Japan. J. Appl. Phys.* **42** L866–8
- Olivo A and Speller R 2007 Modelling of a novel x-ray phase contrast imaging technique based on coded apertures *Phys. Med. Biol.* **52** 6555–73
- Pfeiffer F *et al* 2008 Hard-x-ray dark-field imaging using a grating interferometer *Nat. Mater.* **7** 134–7
- Pfeiffer F *et al* 2007 Hard x-ray phase tomography with low-brilliance sources *Phys. Rev. Lett.* **98** 108105
- Wen H H *et al* 2010 Single-shot x-ray differential phase-contrast and diffraction imaging using two-dimensional transmission gratings *Opt. Lett.* **35** 1932
- Yadav S *et al* 2016 Evaluation of image deblurring techniques *Int. J. Comput. Appl. Technol.* **139** 32–6
- Zanette I *et al* 2014 Speckle-based x-ray phase-contrast and dark-field imaging with a laboratory source *Phys. Rev. Lett.* **112** 1–5